APL Photonics

Development of site-controlled quantum dot arrays acting as scalable sources of indistinguishable photons

Cite as: APL Photonics **5**, 096107 (2020); https://doi.org/10.1063/5.0013718
Submitted: 13 May 2020 . Accepted: 30 August 2020 . Published Online: 17 September 2020

Jan Große, Martin von Helversen, Aris Koulas-Simos, Martin Hermann, and Stephan Reitzenstein

Development of site-controlled quantum dot arrays acting as scalable sources of indistinguishable photons

Cite as: APL Photon. 5, 096107 (2020); doi: 10.1063/5.0013718
Submitted: 13 May 2020 • Accepted: 30 August 2020 •
Published Online: 17 September 2020

Jan Große, Martin von Helversen, Aris Koulas-Simos, Martin Hermann, and Stephan Reitzenstein[a]

AFFILIATIONS

Institut für Festkörperphysik, Technische Universität Berlin, Hardenbergstraße 36, D-10623 Berlin, Germany

[a]Author to whom correspondence should be addressed: stephan.reitzenstein@physik.tu-berlin.de

ABSTRACT

We report on the realization of an array of 28 × 28 mesas with site-controlled InGaAs quantum dots acting as single-photon sources for potential applications in photonic quantum technology. The site-selective growth of quantum dots is achieved by using the buried stressor approach where an oxide aperture serves as the nucleation site in the center of each mesa. Spectroscopic maps demonstrate the positioning of quantum dots with an inhomogeneous broadening of the ensemble emission of only 15.8 meV. Individual quantum dots are characterized by clean single-quantum-dot spectra with narrow exciton, biexciton, and trion lines, with a best value of 27 μeV and an ensemble average of 120 μeV. Beyond that, Hanbury Brown and Twiss and Hong-Ou-Mandel measurements validate the quantum nature of emission in terms of high single-photon purity and photon indistinguishability with a $g^{(2)}(0)$ value of (0.026 ± 0.026) and a post-selected two-photon interference visibility V = (87.1 ± 9.7)% with an associated coherence time of τ_c = (194 ± 7) ps.

I. INTRODUCTION

Quantum devices based on self-assembled semiconductor quantum dots (QDs) are promising building blocks for applications in photonic quantum technology.[1–5] Until now, these quantum emitters have been studied mainly regarding their fundamental optical properties in proof-of-principle experiments, in which they showed close-to-ideal characteristics in terms of on-demand emission of indistinguishable photons and entangled photon pairs with small emission linewidths.[6–10] More recently, the application relevance of QD-based single-photon sources (SPS) has been demonstrated by developing fiber-coupled stand-alone devices.[11,12]

Interestingly, despite the huge progress in the field, the scalable fabrication of regular arrays of high-quality QDs as single-photon emitters still remains a severe technological challenge. Scalability, which is considered a major benefit of semiconductor devices, has so far been hindered for single-QD devices by the randomness introduced in the self-assembled Stranski–Krastanow growth process.[13] In this context, *in situ* lithography techniques have been developed and applied to ensure the deterministic integration of single QDs into quantum light sources with a high process yield.[14–16] However, these devices still rely on integrating self-assembled QDs with random position limiting the scalability of this approach. To overcome these issues, the site-controlled growth of QDs is highly attractive as it allows for realizing arrays of single-photon emitters for large-scale device integration and systems with high quantum functionality. For instance, they could be used for quantum computing concepts relying on highly ordered QD arrays as the nanophotonic substrate for a layered quantum computing architecture.[17]

Several methods for the site-controlled growth of InGaAs QDs have been developed. These methods include the epitaxial growth of QDs at the apex of inverted pyramids on GaAs (111),[18–23] QD formation on etched nano-hole arrays defined by electron beam lithography (EBL),[24,25] and by atomic force microscopy assisted surface oxidation.[26] The nano-hole approach has been quite popular because of its high scalability and its potential for device integration.[27,28] However, nano-holes only cause a short range modification to the chemical potential at the adjacent sample surface, limiting the thickness of the GaAs buffer between the nano-holes and the QD

layer to ~20 nm.[26,29] As a consequence, the QDs are in close proximity to defects at the etched surface of the nano-holes leading to moderate quantum efficiency and pronounced inhomogeneous broadening of single-QD emission lines even in stacked layers of site-controlled quantum dots (SCQDs).[28,30] This problem can be mediated by introducing thicker buffer layers between the nano-holes and the SCQDs, however, at the cost of a lower occupation probability of the pre-defined sites.[31] Another issue of the listed methods is the need for complex marker-based EBL processing for deterministic device integration.

In this work, the site-selective growth of high-quality QD arrays is realized by using the buried stressor approach.[32,33] In this growth concept, a buried AlAs layer undergoes wet thermal oxidation to form Al_2O_3, reducing its volume. The partial oxidation of the AlAs layer leads to a local strain modulation of the surrounding GaAs layers. As self-assembled QD nucleation in the Stranski–Krastanow growth mode is strain-driven, the buried stressor structures can enable deterministic positioning of QDs aligned to oxide apertures formed during the wet thermal oxidation.

An important advantage of the buried stressor method is the absence of etched surfaces close to the SCQDs, leading to an optical quality similar to that of the standard self-assembled InGaAs QDs, as demonstrated, for instance, in resonance fluorescence experiments.[34] Additionally, the UV-lithography based nanostructuring process preceding the oxidation as well as the oxidation itself are highly-scalable and can be done simultaneously and time-effectively on the area of a whole wafer. Furthermore, the oxide aperture is similar to the ones used in vertical-cavity surface-emitting lasers and allows for efficient carrier injection via self-aligned upper contacts.[35]

II. METHOD AND SAMPLE TECHNOLOGY

The sample fabrication involves several nanotechnology processes and two epitaxial growth steps. First, a template sample is grown via metal–organic chemical vapor deposition (MOCVD) on an *n*-doped GaAs (001) substrate. The layer structure consists of a 300 nm GaAs buffer layer, followed by nine alternating layers of 77.8 nm $Al_{0.9}Ga_{0.1}As$ and 66.5 nm GaAs, creating a distributed Bragg reflector (DBR) to increase the photon-extraction efficiency. A 22 nm GaAs layer is then followed by a 30 nm AlAs layer sandwiched between two 45 nm $Al_{0.9}Ga_{0.1}As$ layers including a thin grading layer to reduce stress. The capping GaAs layer has a thickness of 80 nm. All layers are grown at a temperature of 700 °C and an ambient pressure of 100 mbar. The template then undergoes cleanroom processing to expose the AlAs layer for wet thermal oxidation. After thorough surface cleaning, the photo-resist AZ 701 MIR is applied by spin coating. UV lithography is used to pattern the surface with several fields, each consisting of a 28 × 28 array of quadratic mesa structures. The size of the mesas varies from field to field between 19.0 μm and 20.9 μm, and the pitch between individual mesas varies from 30 μm to 60 μm. Subsequently, the mesas are realized by reactive ion etching, which makes the AlAs layer accessible during the following wet thermal oxidation process, as indicated in Fig. 1(a).

The oxidation is performed in a vacuum furnace under a process atmosphere of nitrogen and water vapor at a temperature of 420 °C and a pressure of 50 mbar. The desired aperture size is achieved through *in situ* monitoring of the oxidation fronts via a camera attached to an optical microscope. To stop the oxidation, the chamber is flooded with nitrogen and the heater is turned off. The oxidation process takes around 6 min for a 10 μm mesa and 12 min for a 20 μm mesa. DBR layers that may be exposed by the previous etching are not affected as they contain less than 95% aluminum.

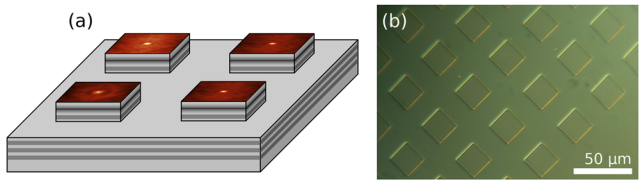

FIG. 1. (a) Schematic of 4 × 4 excerpt from a 28 × 28 mesa array showing the exposed epitaxial layers after the etching process. Darker shades of gray indicate higher aluminum contents of the AlGaAs. Superimposed on the mesa surface are atomic force microscopy (AFM) pictures taken on oxidized mesas with the changes in surface morphology mirroring the strain field in the mesa center caused by the oxide aperture. (b) Optical microscopy images of parts of a mesa array taken with interference contrast after the second MOCVD growth.

Before the QD growth, the buried stressor template structure undergoes a cleaning step in which surface oxides are removed by dipping in 75% sulfuric acid. This is followed by a second MOCVD step, in which, first, a second GaAs buffer of 50 nm thickness is grown. Then, an amount of approximately two monolayers of $In_{0.4}Ga_{0.6}As$ is deposited at an ambient temperature of 500 °C and a V/III ratio of 1.3. As the corresponding layer thickness is above the critical thickness of 1.7 monolayers, self-organized, Stranski–Krastanov-like formation of QDs occurs on the pre-strained surface aligned to the buried oxide apertures. After a growth interruption of 20 s, the QDs are capped with a 1.6 nm thick layer GaAs at a low V/III ratio of 0.5 before the sample is heated up again to a temperature of 615 °C to add the final 100 nm thick GaAs layer. A microscopic image of a mesa array with SCQDs is displayed in Fig. 1(b).

III. EXPERIMENTAL SETUP AND OPTICAL CHARACTERIZATION

Optical device characterization was performed by means of high resolution micro-photoluminescence (μPL) spectroscopy at 10 K. The sample is placed onto a motorized x–y–z stage with sub-μm accuracy in each direction. Optical excitation for the pre-characterization of the arrays is realized by using a HeNe laser emitting at 632 nm, which is focused via a microscope objective (NA = 0.4) onto the surface of the sample. An additional x–y–z piezo stage ensures spatial fine adjustment of the microscope objective. The μPL signal of the mesa structures is then collected by the same microscope objective and detected via a grating spectrometer with a spectral resolution of about 30 μeV. The setup is automatized to record the photoluminescence stepwise from a predefined grid of measurement points. This way, a spectral map is recorded in which each pixel is associated with the spectral information from the surface of a targeted mesa in an array.

All 2D μPL map scans were obtained using an excitation power of 3 μW with an exposure time of 500 ms. Figure 2 shows map

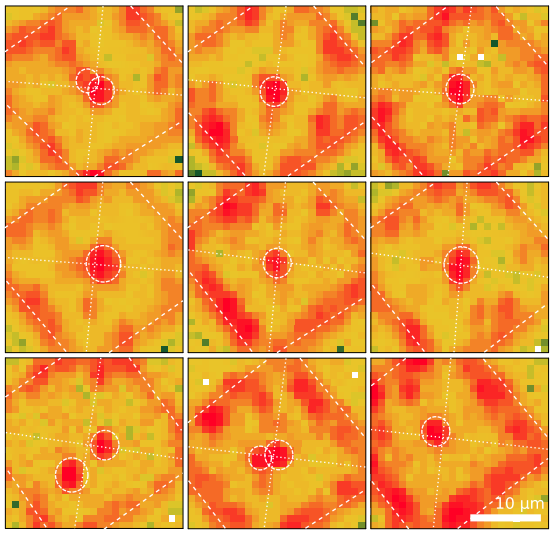

FIG. 2. µPL intensity maps of a 3 × 3 excerpt of a larger 28 × 28 mesa array. All maps show the intensity at the emission window of the central QD or QD ensemble (typically 3 nm in the range of 925 nm–938 nm, varying slightly from mesa to mesa). The edges and the center of each mesa are indicated as well as localized QD emission. QD emission from a 1.5 μm radius from the mesa center is considered as originating from positioned QDs as this is roughly the extend of the local strain modulation caused by the oxide aperture. The color scale is logarithmic on a relative scale with green indicating low and red indicating high emission intensity.

scans from an excerpt of 3 × 3 mesas from the larger 28 × 28 mesa array. To assess the success and accuracy of the QD positioning, the emission intensity in a spectral window corresponding to an emission range between 920 nm and 945 nm is evaluated. The corresponding intensity maps reveal that every mesa shows emission from single SCQDs at its center. We would like to point out that non-deterministic QD nucleation occurs mainly at the mesa edge due to a similar strain profile to the mesa center as a result of the surface geometry. The non-positioned QDs that form off-center on top of the mesa show varying distances from the deterministically positioned ones, but are typically separated by 2 μm or more from the center. The number of SQQDs was obtained by counting the number of emission lines observable in the center of the mesas to account for the possibility that more than one SCQD could be formed in close vicinity within one "pixel" of the map. For each QD, we consider two emission lines (X and CX) at low excitation. Presuming this, we found that about one out of three mesas contains more than one SCQDs (mostly two, rarely up to four SCQDs).

To study the emission properties of the SCQDs in more detail, we take a close look at a mesa in the same array as the 3 × 3 excerpt in Fig. 2. Figure 3 shows two respective µPL intensity maps with panel (a) displaying the emission of a deterministically positioned QD in the center of a mesa (spectral range: 929 nm–931 nm), and panel (b) showing the intensity of wetting layer emission (spectral range: 900 nm–910 nm). The position of the QD signal is located (500, 750) nm relative to the mesa center. Interestingly, its position perfectly correlates with a local minimum in the wetting layer emission intensity. This observation well reflects the fact that the QDs effectively

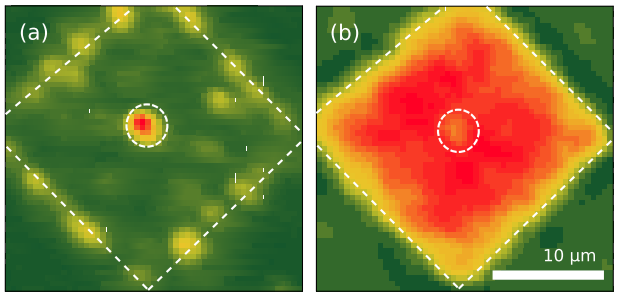

FIG. 3. (a) µPL intensity map of a mesa within QD emission range. (b) µPL intensity map of the same mesa where the intensity is obtained by integrating over the emission from the wetting layer, with the same color scale used as in Fig. 2. The dotted lines indicate the mesa border and the center.

results from a very localized thickness increase of the wetting layer at its position. Consequently, due to the charge carrier transfer into the QD potential, the wetting layer signal intensity at the position of the SCQD decreases. The wetting layer emission, thus, further confirms the successful positioning.

Figure 4(a) shows excitation power dependent µPL spectra of a SCQD from the same mesa array as presented in Figs. 2 and 3. We observe three bright emission lines associated with this QD, which are identified as charged and neutral excitons (CX and X, resp.) and neutral biexciton XX by excitation power and polarization dependent measurements. The measured emission linewidths are 54 μeV for X, 35 μeV for XX, and (resolution limited) 27 μeV for CX, all at an excitation power of 8 μW. To obtain a better understanding of the SCQD quality in the array, we performed an extended statistical analysis by recording and evaluating the optical properties of 100 SCQDs in a 10 × 10 excerpt from the mesa array (including the 3 × 3 subarray in Fig. 2). The corresponding linewidth distribution statistics of the SCQD is displayed in Fig. 4(b) and yields a median linewidth of 107 μeV with the narrowest specimens showing resolution limited single-QD linewidths as low as 27 μeV. Noteworthy, the average linewidth of positioned QDs of 120 μeV is smaller than 160 μeV determined for non-positioned QDs on the etched mesas. This observation may be attributed to the fact that the SCQDs (in the center of the mesas) are located on average farther away from the etched vertical sidewalls of the mesas than the non-positioned ones, which reduced the impact of spectral diffusion due to charge variations of surface states on the QD emission linewidth. Overall, the optical quality of our buried stressor SCQDs in terms of emission linewidth is very promising with about half of our SCQDs exhibiting narrower emission lines than SCQDs fabricated by other determinsitic growth techniques with emission linewidths typically larger than 100 μeV.[26,28,29,36,37]

Figure 4(c) presents the wavelength distribution of 300 emission lines (including X, CX, and XX) from SCQDs and 2021 emission lines from non-positioned QDs evaluated in the same 10 × 10 subarray as mentioned above. The mean wavelength is 933.3 nm with a standard deviation of only 6.6 meV corresponding to a FWHM of 15.8 meV. It should be noted that this value is most likely overestimated regarding the ensemble broadening as both X and XX lines are included in the statistics. It is significantly smaller

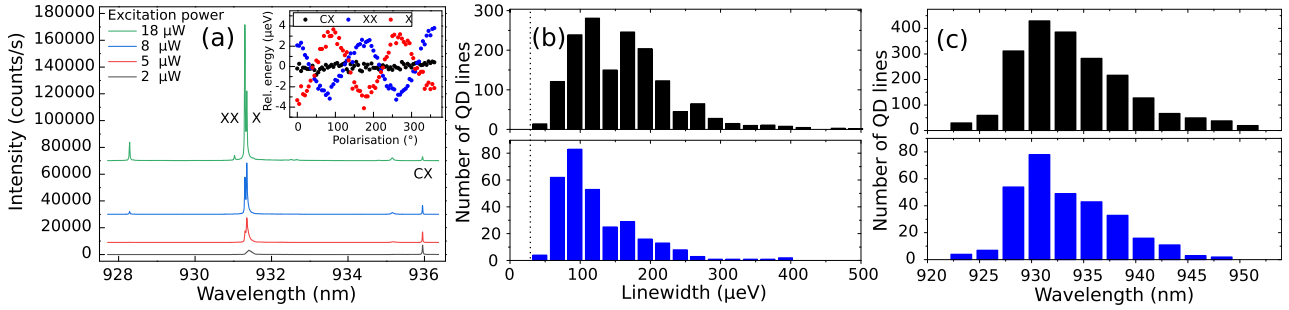

FIG. 4. (a) μPL emission spectra from a SCQD in a mesa center taken at different excitation powers. Emission lines stemming from the excitonic (X), charged excitonic (CX), and biexcitonic state (XX) are marked, respectively. Their polarization dependence is shown in the inset (relative to their mean energy for better visibility). (b) Linewidth distribution statistics of X and XX lines from SCQDs (blue) and non-positioned QDs (black) with average linewidths of 120 μeV and 160 μeV, respectively. The resolution limit is indicated by a dotted black line. (c) Wavelength distribution statistics of SCQDs (blue) and non-positioned QDs (black) fitted by a normal distribution. The fit yields an inhomogeneous broadening of 15.8 meV and 18.4 meV for site-controlled and non-positioned QDs, respectively.

than the inhomogenous broadening of 17.8 meV observed for non-positioned InGaAs QDs in our mesa structures indicating the positive influence of the strain-engineering on the ensemble properties of the SCQDs. The determined inhomogenous broadening of our SCQD is comparable to the values observed for highly homogeneous SCQDs on GaAs (111) with an inhomogeneous broadening ranging from 7.6 meV to 20 meV.[20,36,37]

In order to verify single-photon emission from the SCQDs, we measured the second-order photon-autocorrelation $g^{(2)}(\tau)$ function of emission at 5 K using a fiber-based Hanbury Brown and Twiss (HBT) configuration equipped with superconducting nanowire single-photon detectors (SNSPDs, combined time resolution of two-channel system and electronics: ~100 ps FWHM). First, we studied a SCQD that features stable and bright emission under CW p-shell excitation, provided by a tunable Ti:sapphire laser set to a wavelength of 901.6 nm to match the p-shell energy of this particular dot. The SCQD's neutral biexcitonic emission line at an emission wavelength of 929.6 nm was chosen due to its high brightness and was spectrally filtered by using a monochromator [spectral selection window of 75 μeV (52 pm)]. The corresponding photon-autocorrelation function at saturation of the XX line is presented in Fig. 5(a). The histogram shows pronounced anti-bunching at $\tau = 0$ with an as-measured value of $g^{(2)}_{\mathrm{raw}}(0) = 0.08$. By taking into account the limited temporal resolution of the HBT setup and convoluting it with a double-sided exponential decay,[38] a fit to the data yields a value of $g^{(2)}_{\mathrm{deconv}}(0) = 0.026 \pm 0.026$, thus, proving close to ideal suppression of multi-photon events. Furthermore, to obtain deeper insight into the quantum optical properties of the SCQDs within a statistical analysis, the $g^{(2)}(\tau)$ function was studied for a 4 × 4 excerpt from the 10 × 10 subarray under off-resonant CW excitation (785 nm). For each mesa, one bright and narrow SCQD emission line was chosen, and under the same spectral filtering conditions as above, its second-order autocorrelation function was recorded close to saturation. The resulting deconvoluted values $g^{(2)}_{\mathrm{deconv}}(0)$ are presented in the inset of Fig. 5(a) together with the corresponding decay times τ_{decay} of the exponential fits. In addition, the type of the originating state (X, CX, XX) is indicated, determined by power- and polarization-dependent measurements. As expected, the biexcitonic lines show a smaller time constant, which also explains the comparatively larger errors. The data point with the largest time constant, above 1 ns, was on the other hand a very noisy measurement due to a low signal to noise ratio. All 16 measured QDs show a clear suppression of multi-photon events with

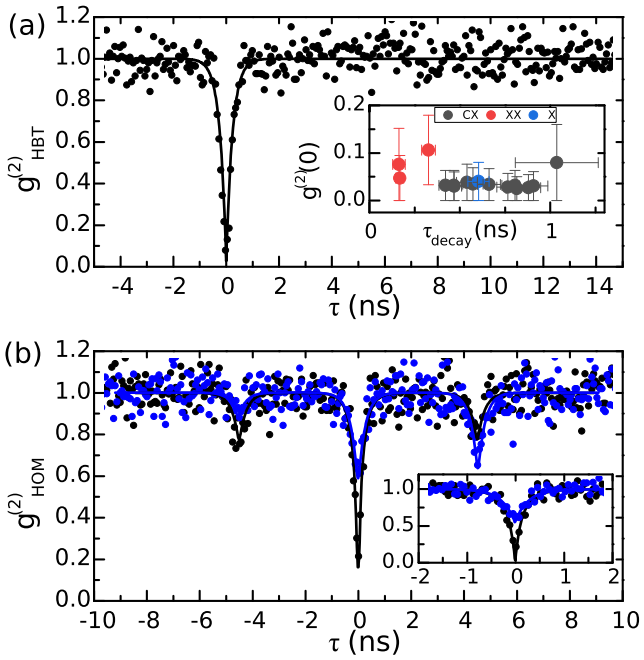

FIG. 5. (a) Typical $g^{(2)}(\tau)$ histogram as measured with an HBT setup from a SCQD under continuous wave p-shell excitation (dots) and the corresponding deconvoluted fit (solid line) yielding $g^{(2)}_{\mathrm{deconv}}(0) = 0.026 \pm 0.026$. The inset shows the results of a statistical analysis of SCQDs in a 4 × 4 excerpt under off-resonant excitation in terms of their deconvoluted $g^{(2)}_{\mathrm{deconv}}(0)$ and the corresponding decay times τ_{decay} of the fit. (b) Corresponding $g^{(2)}(\tau)$ to the same QD as in panel (a) under p-shell excitation with a HOM setup under co-polarized (black dots) and cross-polarized (blue dots) configuration together with the respective convoluted fits (solid lines) leading to a HOM visibility $V_{\mathrm{deconv}} = (87.1 \pm 9.7)\%$ and a coherence time of $\tau_c = (194 \pm 7)$ ps. The inset shows an enlarged excerpt around $(\tau) = 0$ with the deconvoluted fits (solid lines).

only one data point being above 10%, highlighting good quantum optical properties of the buried-stressor SCQDs.

Beyond proving the quantum nature of emission in terms of multi-photon suppression, the photon indistinguishability plays an important role in possible applications of photonic quantum technology. The indistinguishability of photons emitted by the realized SCQDs was evaluated by measuring the two-photon interference (TPI) of subsequently emitted photons from a single QD with a Hong-Ou-Mandel (HOM)-type setup.[39] Using the same QD as for the HBT measurement, again under quasi-resonant excitation, the biexcitonic emission was now coupled to an unbalanced Mach–Zehnder interferometer. A time difference of $\Delta\tau = 4$ ns between the two arms was chosen, which has been shown to be shorter or on the time scale of the decrease in TPI-visibility due to the spectral diffusion in a similar system.[40] The interferometer is single-mode fiber based, and a control measurement can be carried out by changing the polarization of the photons in one interferometer arm and, therefore, rendering the photons distinguishable. Figure 5(b) shows the results and corresponding convolved and deconvolved fits for the co-polarized $[g_{\parallel}^{(2)}(\tau)]$ and cross-polarized $[g_{\perp}^{(2)}(\tau)]$ configurations, again taking into account the time resolution of our setup. The asymmetry of $g_{\perp}^{(2)}(\tau)$ at $\pm\Delta\tau$ is attributed to the meandered design of the SNSPDs, which is the reason for an intrinsic polarization-dependent detection efficiency. Yet, this has no effect on the ratio of the central dips of the two measurements at $\tau = 0$, from which a raw visibility of $V_{raw} = 65.4\%$ and, subsequently, a deconvoluted visibility of $V_{deconv} = (87.1 \pm 9.7)\%$ can be extracted.[38] The fit to $g_{\parallel}^{(2)}(\tau)$ further yields a coherence time of $\tau_c = (194 \pm 7)$ ps. The measured TPI-visibility from our SCQD mesa array surpasses the one from QD arrays where the deterministic positioning is achieved via electron beam nanohole patterning.[31] In addition, an about five-times longer two-photon coherence time is seen in the HOM-dip at zero time delay. Yet, as also stated in the same reference, this could be attributed to their pulsed excitation scheme. It should further be noted that all our values are achieved without the use of a photonic cavity.[7,8]

IV. SUMMARY AND CONCLUSION

In summary, we demonstrate that the buried stressor approach is an attractive method to realize arrays of site-controlled InGaAs QDs with highly selective QD growth. The SCQDs feature a small inhomogeneous broadening of 15.8 meV and an average emission linewidth of 120 μeV with resolution limited values as low as 27 μeV, as determined by an extended statistical analysis including 100 SCQDs from a 10 × 10 excerpt of the fabricated 28 × 28 array. Photon statistics measured in HBT- and HOM-type experiments confirm strong multi-photon suppression with a fitted value of $g_{deconv}^{(2)}(0) = 0.026 \pm 0.026$ and high post-selected indistinguishability expressed in a deconvoluted visibility of $V_{deconv} = (87.1 \pm 9.7)\%$ and a coherence time of $\tau_c = (194 \pm 7)$ ps under p-shell excitation, where the high multi-photon suppression was confirmed in a statistical analysis including 16 SCQDs of a 4 × 4 subarray. Therefore, our site-controlled QD arrays constitute an attractive platform for quantum applications relying on regular arrays of single-photon emitters. As a further improvement of the arrays, it would be interesting to increase the density by reducing the pitch and size of the mesas. In addition, a more careful calibration of the QD density could be used to further increase the selectivity of the site-controlled growth and prevent any unintentional QD growth on the mesa surface except in the center.

AUTHORS' CONTRIBUTIONS

J.G. and M.v.H. contributed equally to this work.

ACKNOWLEDGMENTS

The research leading to these results received funding from the Volkswagen Foundation via NeuroQNet and from the German Research Foundation via Grant No. CRC 787. The authors thank Tobias Heindel and his group for technical support and access to the SNSPD system.

DATA AVAILABILITY

The data that support the findings of this study are available from the corresponding author upon reasonable request.

REFERENCES

[1] J. Loredo, M. Broome, P. Hilaire, O. Gazzano, I. Sagnes, A. Lemaitre, M. Almeida, P. Senellart, and A. White, "Boson sampling with single-photon Fock states from a bright solid-state source," Phys. Rev. Lett. **118**, 130503 (2017).
[2] F. Basso Basset, M. B. Rota, C. Schimpf, D. Tedeschi, K. D. Zeuner, S. F. Covre da Silva, M. Reindl, V. Zwiller, K. D. Jöns, A. Rastelli, and R. Trotta, "Entanglement swapping with photons generated on demand by a quantum dot," Phys. Rev. Lett. **123**, 160501 (2019).
[3] M. Zopf, R. Keil, Y. Chen, J. Yang, D. Chen, F. Ding, and O. G. Schmidt, "Entanglement swapping with semiconductor-generated photons violates bell's inequality," Phys. Rev. Lett. **123**, 160502 (2019).
[4] Z.-H. Xiang, J. Huwer, R. M. Stevenson, J. Skiba-Szymanska, M. B. Ward, I. Farrer, D. A. Ritchie, and A. J. Shields, "Long-term transmission of entangled photons from a single quantum dot over deployed fiber," Sci. Rep. **9**, 4111 (2019).
[5] H. Wang, J. Qin, X. Ding, M.-C. Chen, S. Chen, X. You, Y.-M. He, X. Jiang, L. You, Z. Wang, C. Schneider, J. J. Renema, S. Höfling, C.-Y. Lu, and J.-W. Pan, "Boson sampling with 20 input photons and a 60-mode interferometer in a 10^{14}-dimensional Hilbert space," Phys. Rev. Lett. **123**, 250503 (2019).
[6] A. V. Kuhlmann, J. H. Prechtel, J. Houel, A. Ludwig, D. Reuter, A. D. Wieck, and R. J. Warburton, "Transform-limited single photons from a single quantum dot," Nat. Commun. **6**, 8204 (2015).
[7] N. Somaschi, V. Giesz, L. De Santis, J. C. Loredo, M. P. Almeida, G. Hornecker, S. L. Portalupi, T. Grange, C. Antón, J. Demory, C. Gómez, I. Sagnes, N. D. Lanzillotti-Kimura, A. Lemaítre, A. Auffeves, A. G. White, L. Lanco, and P. Senellart, "Near-optimal single-photon sources in the solid state," Nat. Photonics **10**, 340 (2016).
[8] H. Wang, Z.-C. Duan, Y.-H. Li, S. Chen, J.-P. Li, Y.-M. He, M.-C. Chen, Y. He, X. Ding, C.-Z. Peng, C. Schneider, M. Kamp, S. Höfling, C.-Y. Lu, and J.-W. Pan, "Near-transform-limited single photons from an efficient solid-state quantum emitter," Phys. Rev. Lett. **116**, 213601 (2016).
[9] L. Schweickert, K. D. Jöns, K. D. Zeuner, S. F. Covre da Silva, H. Huang, T. Lettner, M. Reindl, J. Zichi, R. Trotta, A. Rastelli, and V. Zwiller, "On-demand generation of background-free single photons from a solid-state source," Appl. Phys. Lett. **112**, 093106 (2018).
[10] J. Liu, R. Su, Y. Wei, B. Yao, S. F. C. d. Silva, Y. Yu, J. Iles-Smith, K. Srinivasan, A. Rastelli, J. Li, and X. Wang, "A solid-state source of strongly entangled photon pairs with high brightness and indistinguishability," Nat. Nanotechnol. **14**, 586–593 (2019).
[11] A. Schlehahn, S. Fischbach, R. Schmidt, A. Kaganskiy, A. Strittmatter, S. Rodt, T. Heindel, and S. Reitzenstein, "A stand-alone fiber-coupled single-photon source," Sci. Rep. **8**, 1340 (2018).

[12]A. Musial, K. Zolnacz, N. Srocka, O. Kravets, J. Große, J. Olszewski, K. Poturaj, G. Wojcik, P. Mergo, K. Dybka, M. Dyrkacz, M. Dlubek, K. Lauritsen, A. Bülter, P.-I. Schneider, L. Zschiedrich, S. Burger, S. Rodt, W. Urbanczyk, G. Sek, and S. Reitzenstein, "Plug and play fiber-coupled 73 kHz single-photon source operating in the telecom o-band," Adv. Quantum Technol. **3**, 2000018 (2020).
[13]I. N. Stranski and L. Krastanow, "Zur theorie der orientierten ausscheidung von ionenkristallen aufeinander," Monatsh. Chem. **71**, 351–364 (1937).
[14]A. Dousse, L. Lanco, J. Suffczyński, E. Semenova, A. Miard, A. Lemaître, I. Sagnes, C. Roblin, J. Bloch, and P. Senellart, "Controlled light-matter coupling for a single quantum dot embedded in a pillar microcavity using far-field optical lithography," Phys. Rev. Lett. **101**, 267404 (2008).
[15]L. Sapienza, M. Davanço, A. Badolato, and K. Srinivasan, "Nanoscale optical positioning of single quantum dots for bright and pure single-photon emission," Nat. Commun. **6**, 7833 (2015).
[16]M. Gschrey, A. Thoma, P. Schnauber, M. Seifried, R. Schmidt, B. Wohlfeil, L. Krüger, J.-H. Schulze, T. Heindel, S. Burger, F. Schmidt, A. Strittmatter, S. Rodt, and S. Reitzenstein, "Highly indistinguishable photons from deterministic quantum-dot microlenses utilizing three-dimensional in situ electron-beam lithography," Nat. Commun. **6**, 7662 (2015).
[17]N. C. Jones, R. Van Meter, A. G. Fowler, P. L. McMahon, J. Kim, T. D. Ladd, and Y. Yamamoto, "Layered architecture for quantum computing," Phys. Rev. X **2**, 031007 (2012).
[18]S. Watanabe, E. Pelucchi, B. Dwir, M. H. Baier, K. Leifer, and E. Kapon, "Dense uniform arrays of site-controlled quantum dots grown in inverted pyramids," Appl. Phys. Lett. **84**, 2907–2909 (2004).
[19]E. Pelucchi, S. Watanabe, K. Leifer, B. Dwir, and E. Kapon, "Site-controlled quantum dots grown in inverted pyramids for photonic crystal applications," Physica E **23**, 476–481 (2004).
[20]M. H. Baier, S. Watanabe, E. Pelucchi, and E. Kapon, "High uniformity of site-controlled pyramidal quantum dots grown on prepatterned substrates," Appl. Phys. Lett. **84**, 1943–1945 (2004).
[21]G. Juska, V. Dimastrodonato, L. O. Mereni, A. Gocalinska, and E. Pelucchi, "Towards quantum-dot arrays of entangled photon emitters," Nat. Photonics **7**, 527–531 (2013).
[22]G. Juska, V. Dimastrodonato, L. O. Mereni, T. H. Chung, A. Gocalinska, E. Pelucchi, B. Van Hattem, M. Ediger, and P. Corfdir, "Complex optical signatures from quantum dot nanostructures and behavior in inverted pyramidal recesses," Phys. Rev. B **89**, 205430 (2014).
[23]S. T. Moroni, S. Varo, G. Juska, T. H. Chung, A. Gocalinska, and E. Pelucchi, "Vanishing biexciton binding energy from stacked, MOVPE grown, site-controlled pyramidal quantum dots for twin photon generation," J. Cryst. Growth **506**, 36–39 (2019).
[24]P. Atkinson, S. Kiravittaya, M. Benyoucef, A. Rastelli, and O. G. Schmidt, "Site-controlled growth and luminescence of inas quantum dots using *in situ* Ga-assisted deoxidation of patterned substrates," Appl. Phys. Lett. **93**, 101908 (2008).
[25]C. Schneider, M. Strauß, T. Sünner, A. Huggenberger, D. Wiener, S. Reitzenstein, M. Kamp, S. Höfling, and A. Forchel, "Lithographic alignment to site-controlled quantum dots for device integration," Appl. Phys. Lett. **92**, 183101 (2008).
[26]J. Canet-Ferrer, G. Munoz-Matutano, J. Herranz, D. Rivas, B. Alén, Y. Gonzalez, D. Fuster, L. Gonzalez, and J. Martínez-Pastor, "Exciton and multiexciton optical properties of single InAs/GaAs site-controlled quantum dots," Appl. Phys. Lett. **103**, 183112 (2013).
[27]T. Suenner, C. Schneider, M. Strauß, A. Huggenberger, D. Wiener, S. Höfling, M. Kamp, and A. Forchel, "Scalable fabrication of optical resonators with embedded site-controlled quantum dots," Opt. Lett. **33**, 1759–1761 (2008).
[28]A. Huggenberger, S. Heckelmann, C. Schneider, S. Höfling, S. Reitzenstein, L. Worschech, M. Kamp, and A. Forchel, "Narrow spectral linewidth from single site-controlled In(Ga)As quantum dots with high uniformity," Appl. Phys. Lett. **98**, 131104 (2011).
[29]A. Huggenberger, C. Schneider, C. Drescher, S. Heckelmann, T. Heindel, S. Reitzenstein, M. Kamp, S. Höfling, L. Worschech, and A. Forchel, "Site-controlled In(Ga)As/GaAs quantum dots for integration into optically and electrically operated devices," J. Cryst. Growth **323**, 194–197 (2011).
[30]F. Albert, S. Stobbe, C. Schneider, T. Heindel, S. Reitzenstein, S. Höfling, P. Lodahl, L. Worschech, and A. Forchel, "Quantum efficiency and oscillator strength of site-controlled InAs quantum dots," Appl. Phys. Lett. **96**, 151102 (2010).
[31]K. D. Jöns, P. Atkinson, M. Müller, M. Heldmaier, S. M. Ulrich, O. G. Schmidt, and P. Michler, "Triggered indistinguishable single photons with narrow line widths from site-controlled quantum dots," Nano Lett. **13**, 126–130 (2013).
[32]A. Strittmatter, A. Holzbecher, A. Schliwa, J.-H. Schulze, D. Quandt, T. D. Germann, A. Dreismann, O. Hitzemann, E. Stock, I. A. Ostapenko, S. Rodt, W. Unrau, U. W. Pohl, A. Hoffmann, D. Bimberg, and V. Haisler, "Site-controlled quantum dot growth on buried oxide stressor layers," Phys. Status Solidi A **209**, 2411–2420 (2012).
[33]A. Strittmatter, A. Schliwa, J.-H. Schulze, T. D. Germann, A. Dreismann, O. Hitzemann, E. Stock, I. A. Ostapenko, S. Rodt, W. Unrau *et al.*, "Lateral positioning of InGaAs quantum dots using a buried stressor," Appl. Phys. Lett. **100**, 093111 (2012).
[34]M. Strauß, A. Kaganskiy, R. Voigt, P. Schnauber, J.-H. Schulze, S. Rodt, A. Strittmatter, and S. Reitzenstein, "Resonance fluorescence of a site-controlled quantum dot realized by the buried-stressor growth technique," Appl. Phys. Lett. **110**, 111101 (2017).
[35]W. Unrau, D. Quandt, J.-H. Schulze, T. Heindel, T. D. Germann, O. Hitzemann, A. Strittmatter, S. Reitzenstein, U. W. Pohl, and D. Bimberg, "Electrically driven single photon source based on a site-controlled quantum dot with self-aligned current injection," Appl. Phys. Lett. **101**, 211119 (2012).
[36]B. Rigal, C. Jarlov, A. Rudra, P. Gallo, A. Lyasota, B. Dwir, and E. Kapon, "Site-controlled InGaAs/GaAs pyramidal quantum dots grown by MOVPE on patterned substrates using triethylgallium," J. Cryst. Growth **414**, 187–191 (2015).
[37]I. V. Kulkova, A. Lyasota, C. Jarlov, B. Rigal, A. Rudra, B. Dwir, and E. Kapon, "Emission wavelength control of ordered arrays of InGaAs/GaAs quantum dots," J. Cryst. Growth **464**, 69–74 (2017).
[38]R. Patel, A. Bennett, K. Cooper, P. Atkinson, C. Nicoll, D. Ritchie, and A. Shields, "Postselective two-photon interference from a continuous nonclassical stream of photons emitted by a quantum dot," Phys. Rev. Lett. **100**, 207405 (2008).
[39]C. K. Hong, Z. Y. Ou, and L. Mandel, "Measurement of subpicosecond time intervals between two photons by interference," Phys. Rev. Lett. **59**, 2044 (1987).
[40]A. Thoma, P. Schnauber, M. Gschrey, M. Seifried, J. Wolters, J.-H. Schulze, A. Strittmatter, S. Rodt, A. Carmele, A. Knorr, T. Heindel, and S. Reitzenstein, "Exploring dephasing of a solid-state quantum emitter via time- and temperature-dependent Hong-Ou-Mandel experiments," Phys. Rev. Lett. **116**, 033601 (2016).